JOURNAL OF MATERIALS SCIENCE 28 (1993) 203–217

Sintering characteristics of Fe and FeCo alloy ultrafine powders

Y. SAKKA, T. UCHIKOSHI, E. OZAWA*
National Research Institute for Metals, 3-12, Nakameguro-2, Meguro-ku; Tokyo 153, Japan

Sintering characteristics of three kinds of iron and FeCo alloy ultrafine powders (UFPs) in vacuum and a hydrogen atmosphere were examined by continuously measuring their dimensions, and observing their structural changes. The UFPs exposed to air contain mixtures of oxide and hydroxide phases. The oxide phase increased during heating in vacuum. The compacts of the UFPs shrunk slightly at temperatures between 450 and 700 K, where the surface oxides sintered, and then densified rapidly above 700 K. The shrinkage in a stream of hydrogen occurred at much lower temperatures than that in vacuum. The reduction reaction is rate-controlled by an interface reaction and the reduction rate of the UFPs depends on the oxidation level, where the more highly oxidized UFPs tend to the lower reduction rate. Activation energies of the reduction rate constants of the iron UFPs and FeCo UFPs lie in the range 48–59 kJ mol^{-1}.

1. Introduction

Metal ultrafine powders (UFPs) have extremely large specific surface areas and high reactivity. Studies on the utilization of metal UFPs have been conducted as powders, films and bulk materials [1, 2]. Catalysis is a typical example of utilization of powders. Films consisting of UFPs are expected to be excellent sensor materials and electrode materials, etc. A "gas deposition method" for preparing films of UFPs has been developed by Hayashi's group [1]. In the case of the bulk materials, the following three types of study have been carried out: (1) decrease of sintering temperature and time, (2) synthesis of dense nano-sized materials, and (3) synthesis of porous materials.

According to Herring's law [3] and traditional sintering theory [4], the finer the particle size, the lower is the sintering temperature and the shorter is the sintering time. In fact, sintering shrinkage of the clean ultrafine powders (UFPs) occurs at lower temperatures [5, 6]. However, it is difficult to obtain dense products by sintering UFPs, because of their tendency to strongly agglomerate and the evolution of gases [7]. Two types of procedure are reported in the synthesis of their dense bodies. One is the method developed by Gleiter's group [8] and Siegel's group [9] in which the compaction process was conducted *in situ* under a high pressure after preparing UFPs by a gas evaporation technique. The other method was conducted by Hayashi's group [10–12] in which loosely packed UFPs, which had been exposed to air, were reduced, followed by sintering under a pressure of 0–500 MPa.

The fabrication of porous materials by consolidating UFPs is one of the best utilizations of their large specific surface areas. The silver porous materials using a heat exchanger (mK) is the most successful example [13, 14]. In the preparation of these porous materials, the initial sintering characteristics of UFPs are important factors which control the structure of the porous materials.

UFPs are so reactive that the surface of the powders is oxidized and contaminated with large amounts of gases after exposure to air [5, 15, 16]. In addition, hydroxide-like and carbonate-like compounds have been produced during storage [17–19]. To recover the initial reactive surface state, a reduction treatment is necessary. To inhibit the grain growth during this treatment, the reduction temperature must be kept as low as possible. Therefore, we must determine the reduction process of the UFPs. The porous materials might be very reactive as is the case of the metal UFPs. The information on surface reactivity and surface state of the UFPs is quite useful in understanding the treatment and the utilization of the porous materials.

Iron and its intermetallic compounds are well known as excellent catalysis, magnetic materials and structural materials, etc. Therefore, many studies have been conducted to investigate these properties. One means of improving these properties, is by reducing particles or grain sizes. For this, it is necessary to start with UFPs.

In the present study, the sintering characteristics of three kinds of iron and FeCo alloy UFPs in vacuum and a hydrogen atmosphere were examined by various techniques. We have demonstrated that gas desorption measurements are suitable for estimating the

Present address: K. K. L'Air Liquide Laboratories, 5-9-9 Tokodai, Tsukuba-shi, Ibaraki, 300-26, Japan.

surface compounds and structural changes of the UFPs in vacuum [5, 15–19]. The sintering characteristics were discussed with the gas desorption data. Their reduction characteristics in a hydrogen atmosphere were also studied.

2. Experimental procedure

Three kinds of iron UFPs and 60 (at %) Fe–40Co alloy UFPs were prepared by the Vacuum Metallurgical Co. Ltd, using a gas evaporation method [1, 20]. To characterize the as-received UFPs, transmission electron microscopy (TEM) observation, X-ray diffraction (XRD), Mössbauer measurements were conducted.

Specific surface measurements, continuous dimensional change measurements and scanning electron microscopy (SEM) observations were conducted to examine the sintering characteristics. The Brunauer–Emmett–Teller (BET) adsorption technique was used to measure specific surface areas using nitrogen gas as an adsorbate and assuming a cross-sectional area of 0.162 nm^2. The consolidation pressure is an important factor in controlling the final density. In the case of iron UFPs exposed to air, the higher the consolidating pressures, the lower are the sintered densities after heating at 973 K in a hydrogen atmosphere [7]. This phenomenon is due to the gas desorption and the inhomogeneous packing arising from the agglomerated powders [7]. Therefore, in this experiment, all powders were pressed into discs of approximately 6 mm diameter and 3–5 mm thick under a pressure of 30 MPa. The continual change in the dimensions of the pellets was measured using a dilatometer in a vacuum (approximately 10^{-4} torr; 1 torr $\simeq$ 133.322 Pa) and a stream of hydrogen (flow rate 800 ml min^{-1}).

Thermogravimetry (TG) analyses were performed to study the reduction process of the UFPs in a stream of hydrogen. In all experiments, treatment of the UFPs was conducted in a stream of nitrogen or argon gas to avoid contamination with air.

3. Results

3.1. Characterization of as-received powders

The impurity contents of oxygen and carbon of the three kinds of iron and FeCo alloy UFPs are summarized in Table I, together with the specific surface areas which were measured after outgassing at room temperature. The particle shape is spherical as seen in Fig. 1, and the particles form necklace-type structures of hard agglomerates. The particle sizes of the UFPs seen in the transmission electron micrographs are

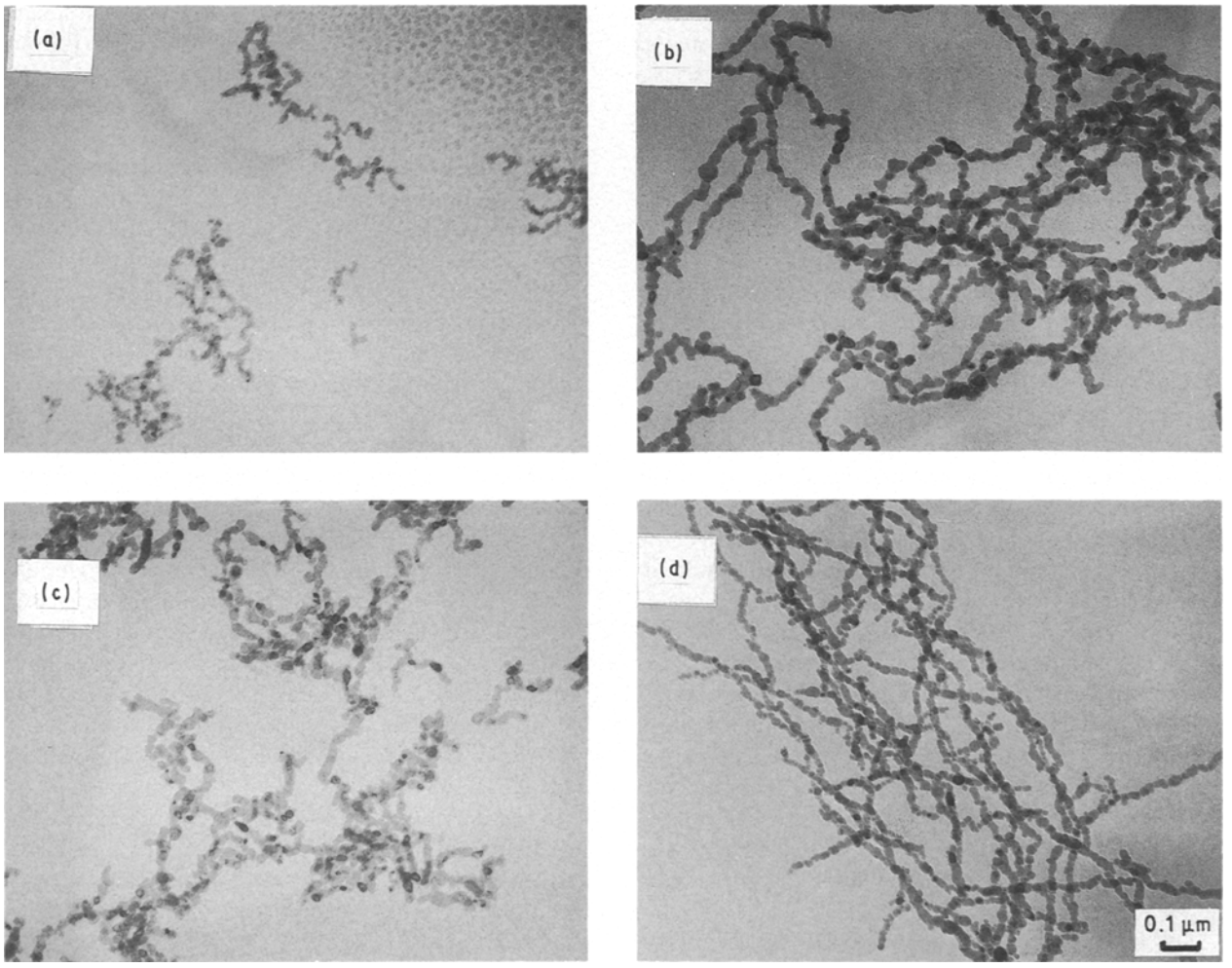

Figure 1 Transmission electron micrographs of the ultrafine powders of (a) Fe1, (b) Fe2, (c) Fe3, and (d) FeCo.

TABLE I Oxygen and carbon impurity contents and specific surface areas of three kinds of iron and FeCo UFPs

Sample	Oxygen (mass %)	Carbon (mass %)	Specific surface areas ($m^2 g^{-1}$)
Fe1	23.3	0.190	54.0
Fe2	15.0	0.083	32.6
Fe3	10.6	0.065	31.8
FeCo	13.0	0.088	37.9

comparable to those calculated from the specific surface areas. The samples of Fe1, Fe2 and FeCo were subjected to a slow oxidation treatment followed by exposure to air. The slow oxidation treatment is generally conducted in flowing gases containing a small amount of oxygen gas [21]. Sample Fe3 was not subjected to such treatment, but contained a large amount of oxygen impurity, which was probably adsorbed when the powders were stored in the sealed sample bottle.

XRD patterns showed that iron UFPs had Fe_3O_4 (or γ-Fe_2O_3) phase besides α-Fe phase. The lattice constants of the oxide phase of Fe1 and Fe2 were 0.8364 and 0.8371 nm, respectively. These values lie between the lattice constants of Fe_3O_4 (0.8396 nm) and that of γ-Fe_2O_3 (0.83515 nm), which indicates that both Fe_3O_4 and γ-Fe_2O_3 phases exist in the iron UFPs as reported by Haneda and Morrish [22]. Furthermore, Fe1 contained α-Fe_2O_3 phase. FeCo had spinel-type $(Fe, Co)_3O_4$ phase in addition to the α-FeCo phase.

The crystallite size was calculated by following Sherrer's equation [23] from the X-ray line broadening using (3 1 1) for cubic oxide and (1 1 0) for metal

$$t = 0.9\lambda/B\cos\theta \quad (1)$$

where t is the crystallite size, λ the wavelength, θ the diffraction angle, and B the angular width. The atomic ratios of oxide and metal phases were determined from the Mössbauer absorption areas [24] measured at room temperature or 77 K. Table II summarizes the crystallite sizes of oxide and metal phases, and their atomic composition.

TABLE II Properties of three kinds of iron and FeCo UFPs

Samples	Crystallite size (nm)[a]		Composition (at %)[b]	
	Metal	Oxide	Metal	Oxide
Fe1	9.4	5.9	32.8	67.2
Fe2	15.7	5.0	63.1	36.9
Fe3	13.0	3.9	[c]	[c]
FeCo	15.4	3.7	73.1	26.9

[a]Determined from line broadening using (3 1 1) for cubic oxide and (1 1 0) for metal.
[b]Obtained from Mössbauer absorption area.
[c]Not measured.

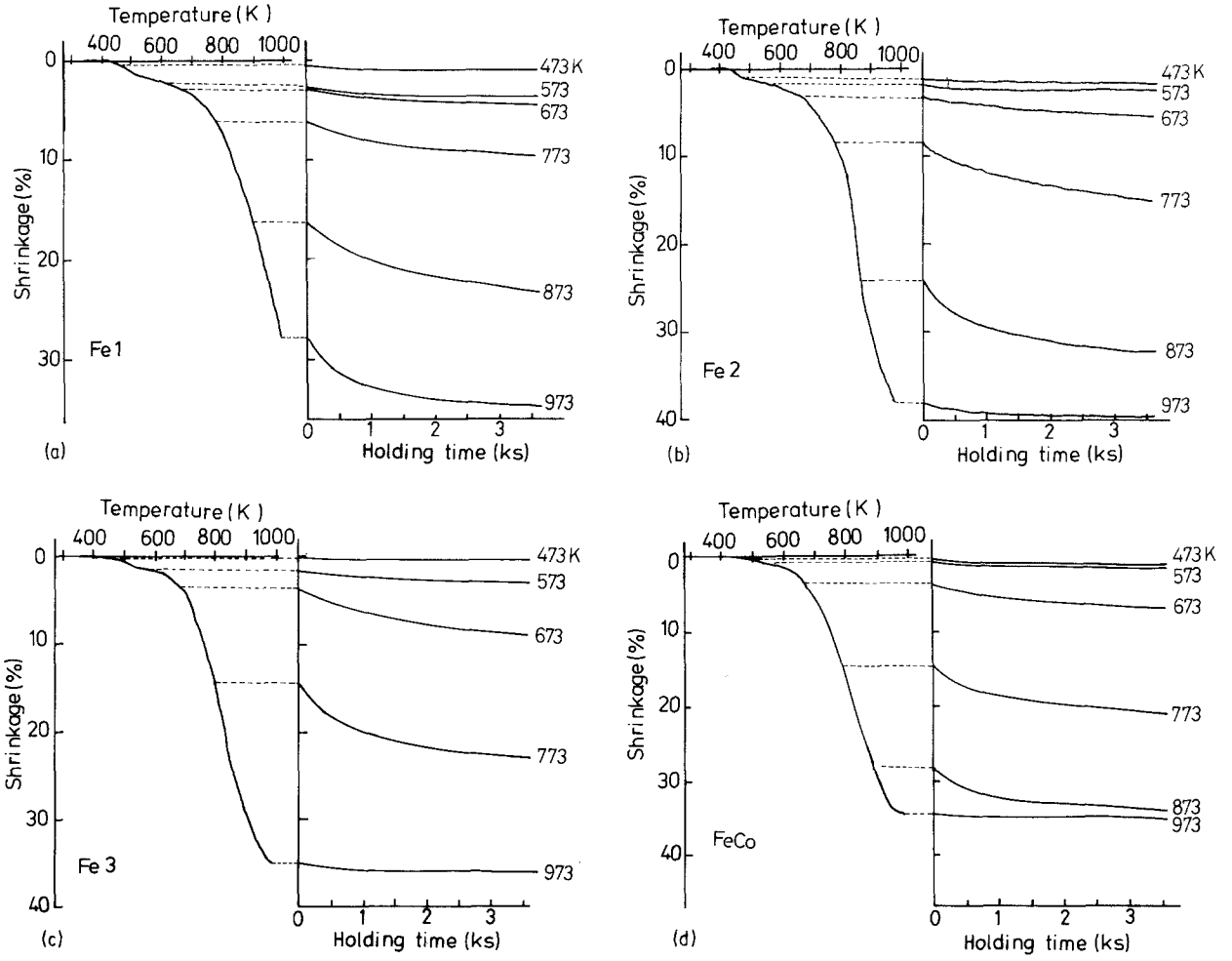

Figure 2 Linear shrinkage of the compacts during heating to fixed temperatures at a heating rate of 5 K min^{-1} (left-hand side), and during isothermal holding (right-hand side) in vacuum. (a) Fe1, (b) Fe2, (c) Fe3, and (d) FeCo.

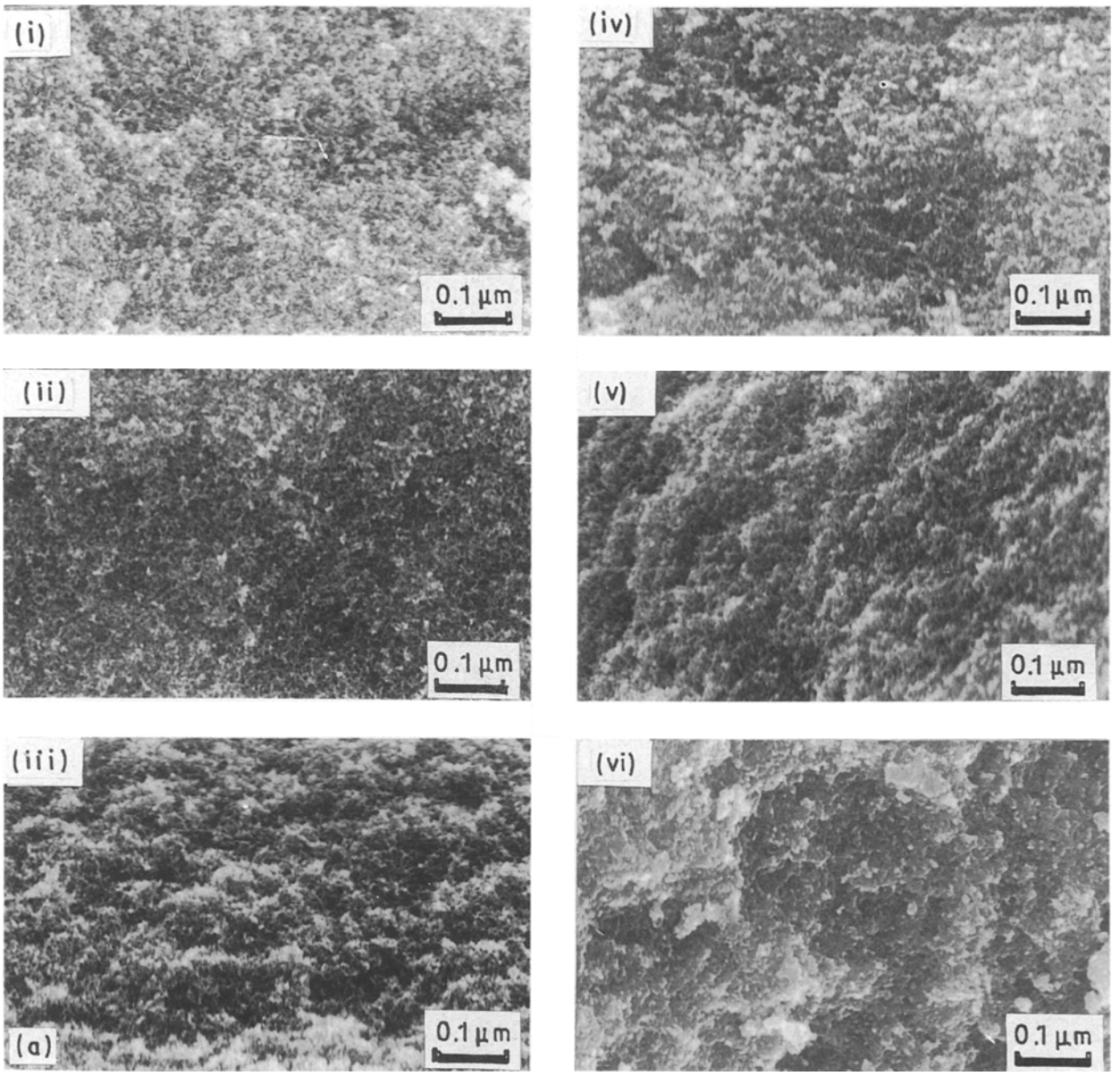

Figure 3 Fractured surfaces of the compacts sintered at (i) 473 K, (ii) 573 K, (iii) 673 K, (iv) 773 K, (v) 873 K and (vi) 973 K in vacuum. (a) Fe1, (b) Fe2, (c) Fe3, and (d) FeCo.

3.2. Sintering in vacuum

The green densities of Fe1, Fe2, Fe3 and FeCo were approximately 1.1, 1.3, 1.6, and 1.4 g cm^{-3}, respectively. Fig. 2 shows the linear shrinkage of the compacts of the UFPs during heating to fixed temperatures (left-hand side) at a heating rate of 5 K min^{-1} and the isothermal holding (right-hand side) in vacuum. The compacts expand slightly around 400 K and shrink during heating. The shrinkage region might be divided into two steps; slight shrinkage (450–700 K) and steep shrinkage (above 700 K) regions. Fig. 3 shows the fractured surfaces of the compacts of Fe1, Fe2, Fe3 and FeCo sintered at fixed temperatures for 3.6 ks. Significant grain growth is observed for the compacts sintered above 873 K.

Fig. 4 shows the variations of specific surface areas after heating at fixed temperatures for 7.2 ks in vacuum. In the temperature range where the expansion is observed in Fig. 2 (around 400 K), the specific surface areas increase or hold constant values, and then decrease slightly.

During heating in vacuum, the oxide phase increased as is shown in Fig. 5. The oxide phases of iron UFPs converted from Fe_3O_4 to FeO after heating 973 K. Fig. 6 shows the X-ray intensity ratio of $(Fe, Co)_3O_4$ (3 1 1) to α-(Fe, Co) (1 1 0). The origin of the increase in oxide phase and the effect of the oxide phase on the sintering will be discussed later in comparison with the gas desorption data.

3.3. Sintering in a hydrogen atmosphere

Fig. 7 shows the linear shrinkage of the compacts of the UFPs during heating to fixed temperatures (left-hand side) at a constant heating rate of 5 K min^{-1} and the isothermal holding (right-hand side) in a stream of hydrogen. The shrinkage in the hydrogen atmosphere is much larger than that in vacuum (dotted line). Fig. 8

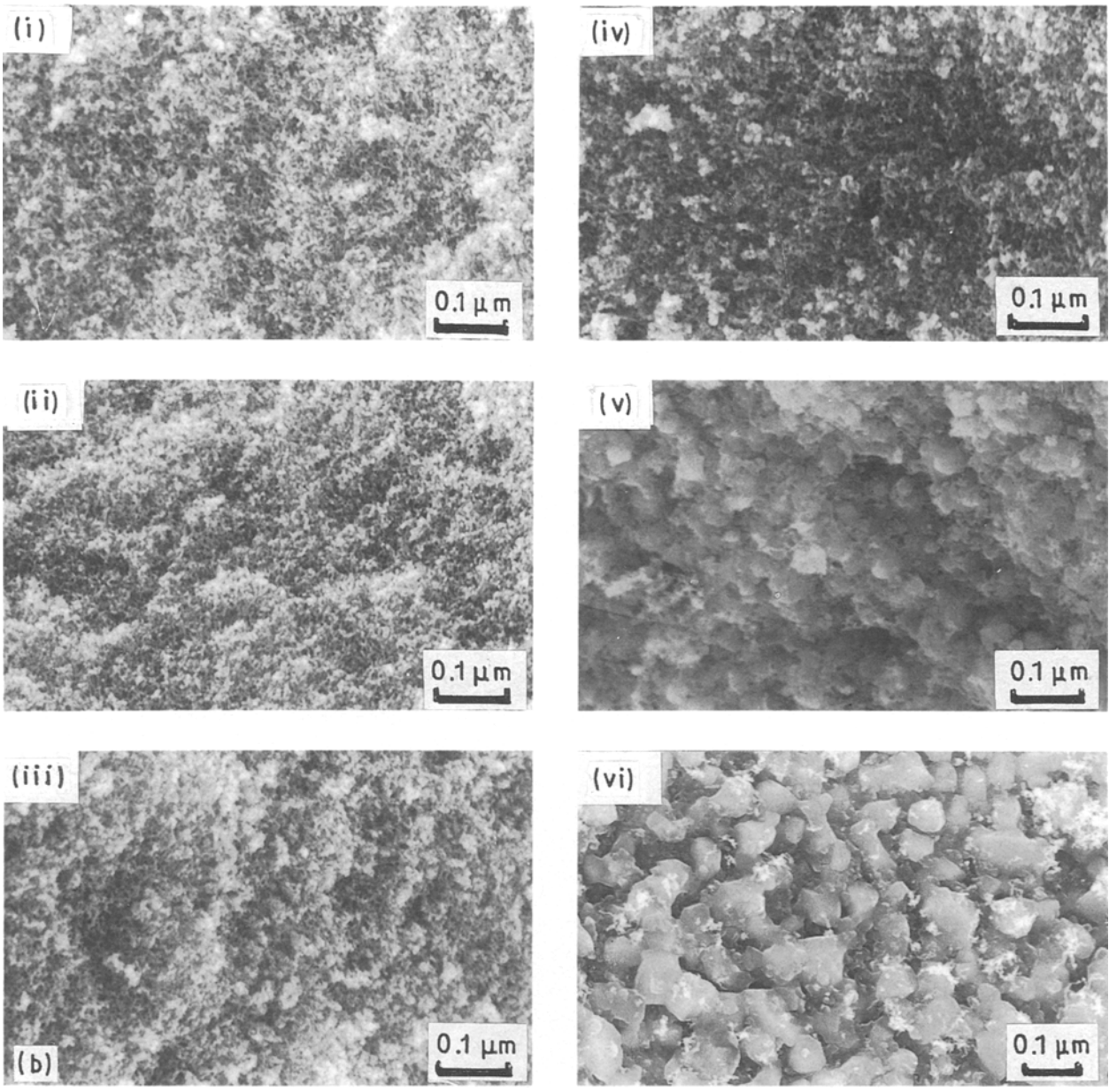

Figure 3 Continued

shows the fractured surfaces of the compacts sintered at fixed temperature for 3.6 ks in a stream of hydrogen. Significant grain growth is observed for the compacts sintered above 673 K.

Fig. 9 shows the TG curves of the UFPs heated at a constant heating rate of 5 K min^{-1} in a stream of hydrogen. The reduction reactions complete at lower temperatures as the oxidation level decreased. Large shrinkage occurred during the reduction reaction. These results show that the clean UFPs sinter at lower temperatures and that the oxide phase hinders the sintering.

4. Discussion

4.1. Structural changes during heating in a vacuum

Oxide phase increases during heating in a vacuum, as stated above. To determine the origin of the increase of oxide, temperature-programmed gas desorption (TPD) measurements were conducted [25, 26]. The TPD measurements are suitable for estimating the surface chemistry and surface reactions of UFPs.

The evolved gases were mainly H_2O, H_2, CO, and CO_2 gases. The temperature-programmed gas desorption spectra of the UFPs have several peaks, as seen in Fig. 10. The peak temperatures of the iron UFPs and those of the FeCo UFPs are similar, which indicate that both UFPs have similar surface structures and similar surface reactions. The three desorption peaks of H_2O were marked as (A) 400–440 K, (B) 520–550 K and (C) 610–640 K, the two desorption peaks of H_2 as (β) 520–540 K and (γ) 590–660 K, and more than five peaks of CO or CO_2 as; (I) 370–380 K, (II) 430–450 K, (III) 490–540 K, (IV) 610–630 K, and (V) above 680 K. These peaks are not explained by the desorption from the metal surface [27]. The UFPs adsorbed many gases on the oxidized surface and might have produced hydroxide-like or carbonate-like compounds during storage, which must have a very

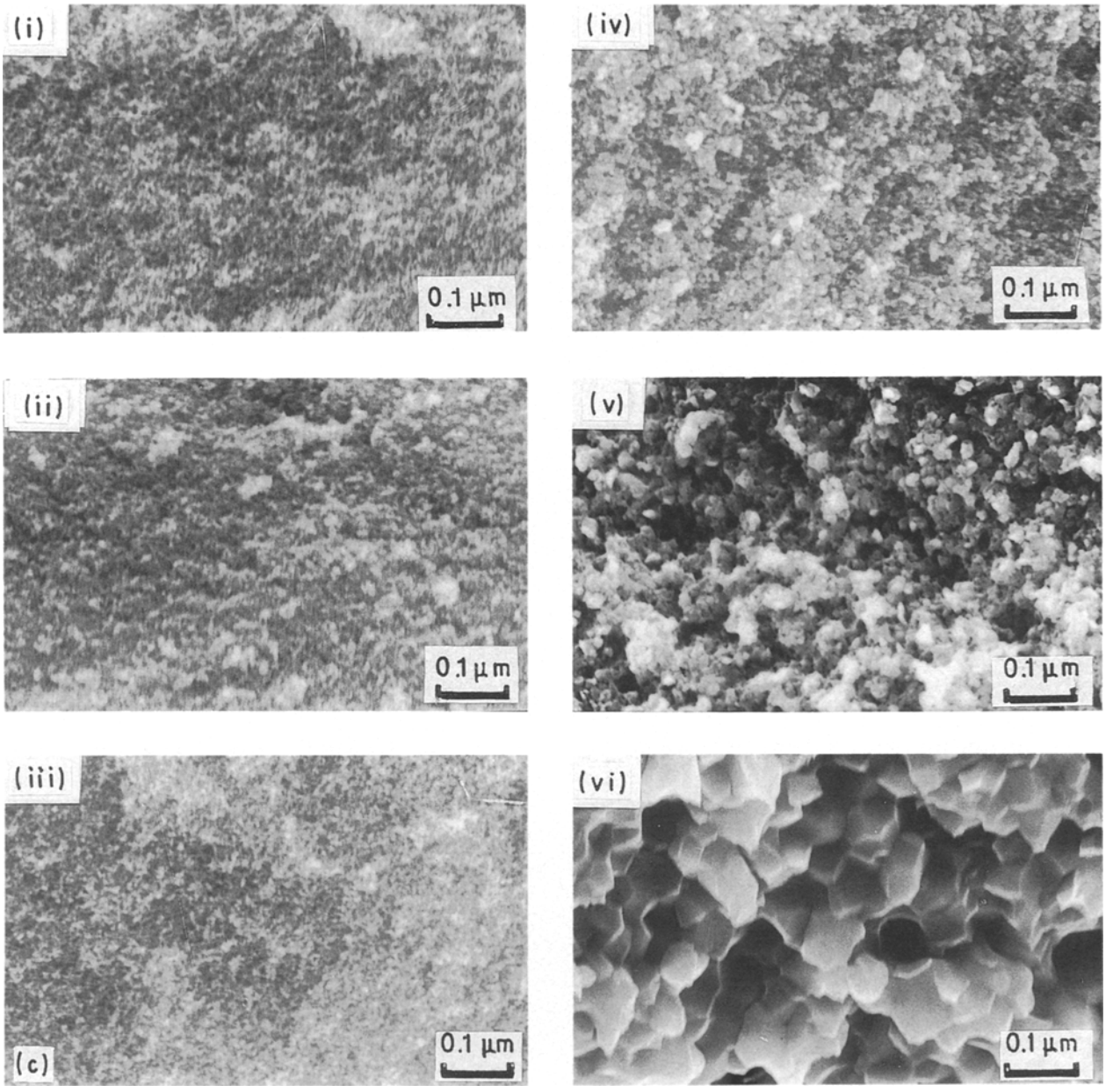

Figure 3 Continued

fine or amorphous structure because they were not confirmed by XRD. To interpret the TPD spectra of the UFPs, TPD measurements of powders of Fe_3O_4, α-Fe_2O_3, γ-Fe_2O_3 and γ-FeOOH were conducted. The H_2O desorption peaks A and C correspond to the temperatures of H_2O desorption from the γ-Fe_2O_3, and the desorption peak B is attributed to the decomposition of γ-FeOOH as seen in Fig. 11. These results imply that the iron UFPs, exposed to air, contained γ-FeOOH on the surface of the oxide phase (Fe_3O_4 and γ-Fe_2O_3). This surface state was also confirmed by ESCA measurements [28].

The H_2 desorption peaks β and γ are closely related to the H_2O desorption peaks B and C, respectively, as judged from the coincidence of the peak temperatures. The H_2 desorption peak β is due to the reaction of metal with the water produced by the decomposition of oxyhydroxide, and the peak γ is due to the desorption from γ-Fe_2O_3. As seen in Fig. 10, the two H_2 desorption intensities differ between Fe1 and the others; in the case of Fe1, the intensity of the β peak is larger than that of γ peak, but in other samples the intensity relation is reverse. This result suggests that in the case of Fe1, which was oxidized significantly, the quantity of the metal phase which contacts the oxyhydroxide is large but that which contacts the γ-Fe_2O_3 is small in the case of Fe1 [25, 29]. This result is quite useful in understanding the corrosion behaviour of iron [29].

Although there are no TPD spectra concerned with FeCo oxide or oxyhydroxide compounds, the surface conditions of the FeCo UFPs might be similar to those of the iron UFPs.

To determine the origin of the desorption CO_2 peaks I and II, the sample of Fe2 was heated to 693 K in vacuum followed by exposure to H_2O at room temperature, and then TPD experiments were conducted. After these treatments, the CO_2 peaks I and II

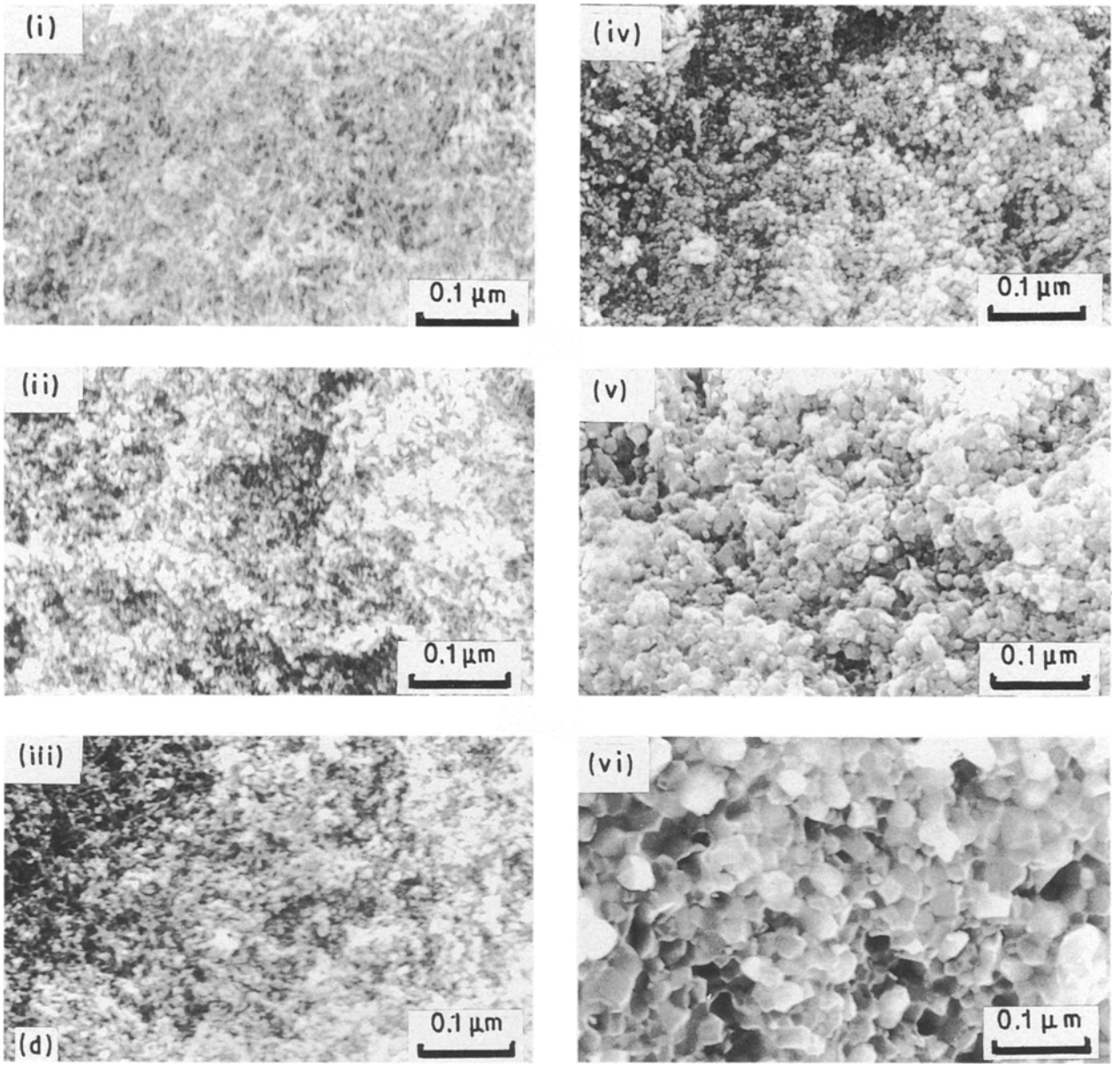

Figure 3 Continued

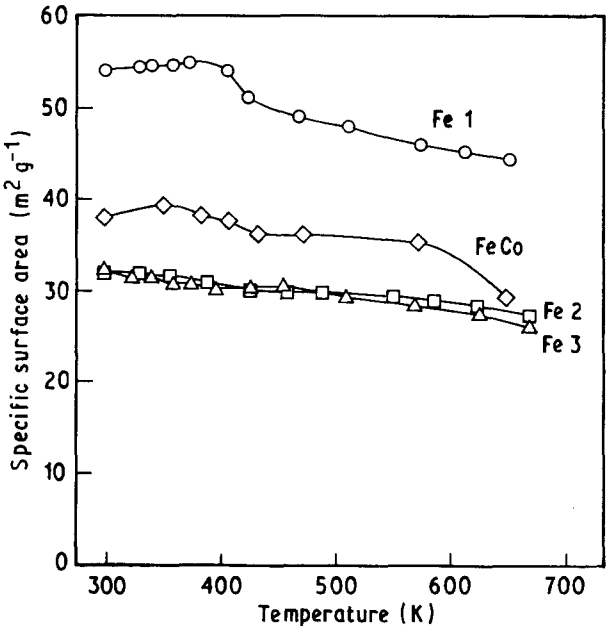

Figure 4 Variations of the specific surface areas of the UFPs after heating at fixed temperatures for 2 h in vacuum.

were not observed. Therefore, the peaks I and II seem to be arising from the adsorbed CO or CO_2 when the UFPs were exposed to air. The CO_2 peaks III and IV are closely related to the H_2O desorption peaks B and C, and to the H_2 desorption peaks β and γ, respectively, by the coincidence of the peak temperatures. These coincidences suggest that these peaks originate from the same sources. The CO_2 desorption III and IV has arisen from the reaction of carbon impurity with the desorption H_2O. The CO_2 peaks above 680 K have arisen from the reaction of carbon impurity with the oxygen [25].

From the above results, the following three reasons are considered to be why the oxide phase increased during heating in vacuum. First, oxidation is caused by the adsorbed gases ((OH) (ad), O (ad), CO (ad), etc.) on the oxide surface of the UFPs. For example, the desorption of H_2O is expressed as follows.

$$2(OH)(ad) \rightarrow H_2O(gas) + O(ad) \quad (2)$$

The produced O(ad) accompanied by the H_2O desorption is considered to contribute further to the

oxidation. Second, an oxide phase is produced by the decomposition of hydroxide-like and carbonate-like compounds. Third, an oxide is produced by the following reaction

$$4H_2O + 3(Fe,Co) \rightarrow (Fe,Co)_3O_4 + 4H_2 \quad (3)$$

where the evolution of water arises form Reaction 2 and the decomposition of the oxyhydroxide phase.

4.2. Reduction kinetics in a hydrogen atmosphere

Fig. 12 shows examples of the weight losses of Fe2 and FeCo during isothermal holding in a stream of hydrogen. The heating time to fixed temperatures was 600 s. The reduction process of Fe_3O_4 is known to be rate-controlled initially by the interface reaction and then later by the diffusion. The reduction rate by the inter-

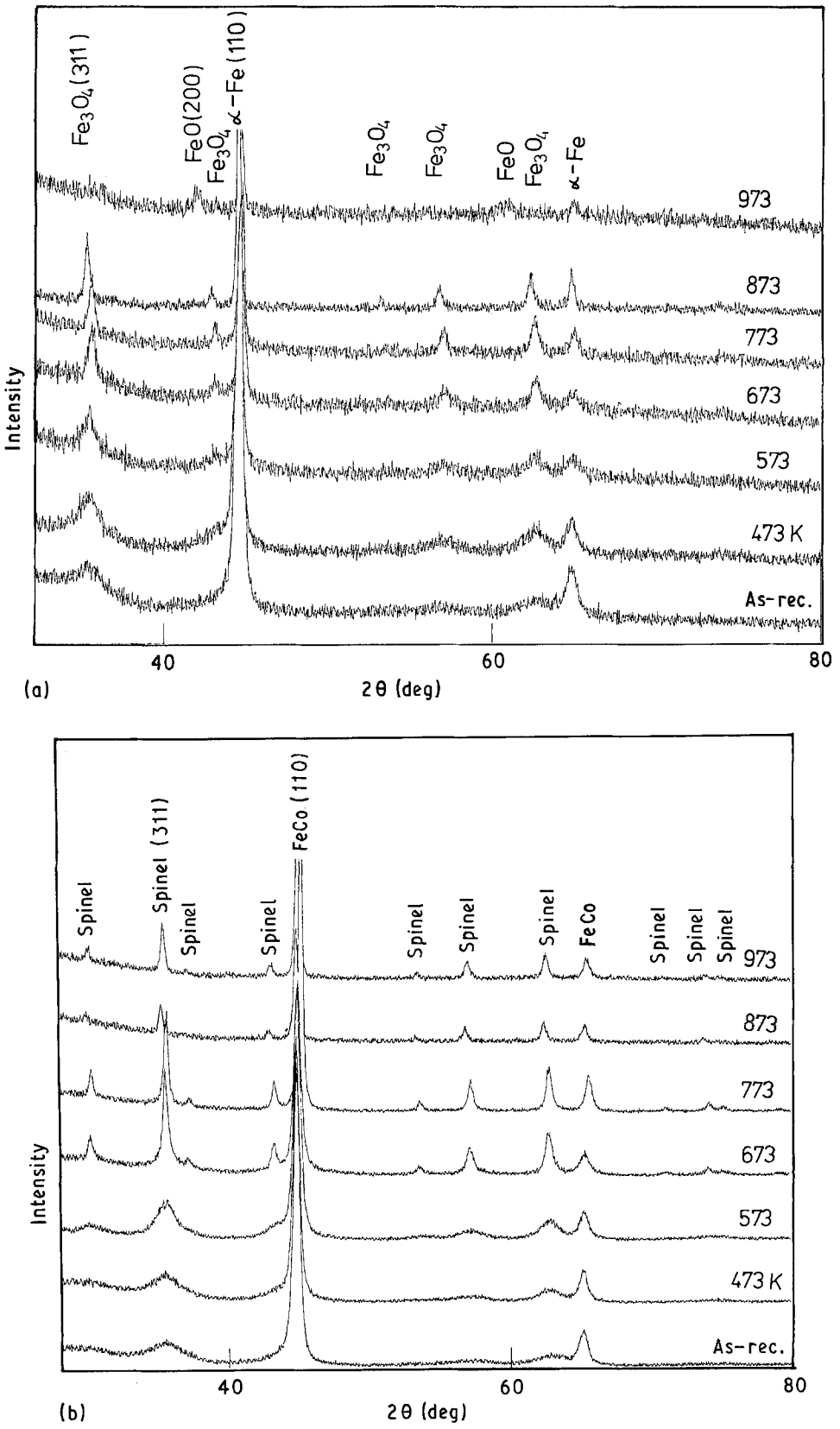

Figure 5 X-ray diffraction patterns of (a) Fe2 and (b) FeCo after heating at fixed temperatures for 1 h in vacuum.

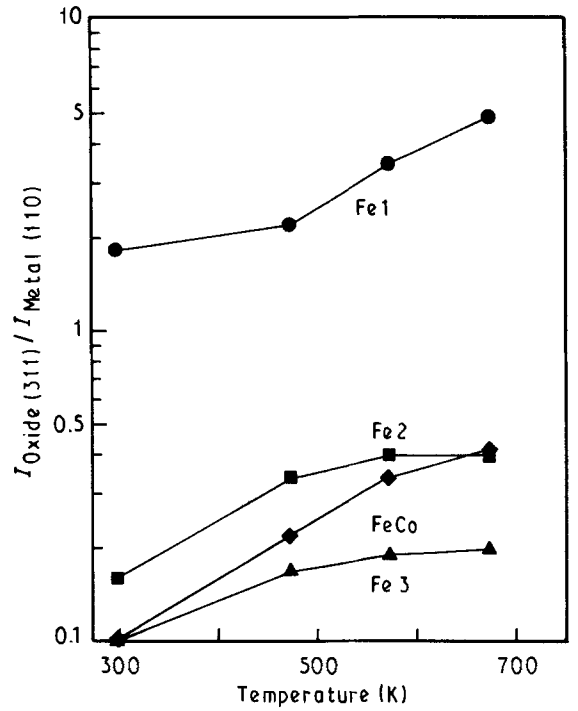

Figure 6 X-ray intensity ratio of (Fe, Co)$_3$O$_4$ (3 1 1) to α-(Fe, Co) (1 1 0) after heating at fixed temperatures for 1 h in vacuum.

face reaction is expressed as follows [30].

$$[1 - (1 - R)^{1/3}] = K't/(r_0 d_0) = Kt \quad (4)$$

where r_0 and d_0 are initial radius and density of the oxide, respectively, R the reduction ratio, K' the rate constant, and t the reduction time. Fig. 13 shows the relation of $[1 - (1 - R)^{1/3}]$ versus time. Although an incubation period is observed in the first stage in the case of FeCo UFPs, it is seen that the reduction reaction of the UFPs proceeds almost by the interface reaction. Fe1 also showed an incubation period, as is the case for FeCo, before the reduction by the interface reaction [25]. No region controlled by the diffusion process is significantly observed, probably because the crystallite of the oxide is very small. Fig. 14 shows the Arrhenius plots of the UFPs. The data of Fe3 were omitted because its surface was so reactive that some oxidation reaction could occur during treatment and the oxidation level might change in each TG experiment.

The magnitude of the rate constants seems to depend on the oxidation level of the UFPs. As seen from Equation 4, the rate constant depends on the initial radius and the densities of the oxide. The initial radius corresponds to the crystallite sizes of the oxide phase as shown in Table II. The higher oxidation level, the larger is the crystallite size. However, the large difference in the rate constant cannot be explained solely by the difference in the crystallite size. Therefore, the density difference (the higher the oxidation level, the higher is the density of the oxide) also contributes to the difference in the rate constant. The activation energies of the reduction rate constants of Fe1, Fe2 and FeCo are 54, 59 and 48 kJ mol^{-1}, respectively. These values are comparable to the reported values (54–67 kJ mol^{-1}) of the interface-reaction controlled reduction reaction of Fe_3O_4 below 843 K [31].

4.3. Sintering characteristics

It is difficult to observe microstructural changes of the UFPs at lower temperatures in vacuum. We have

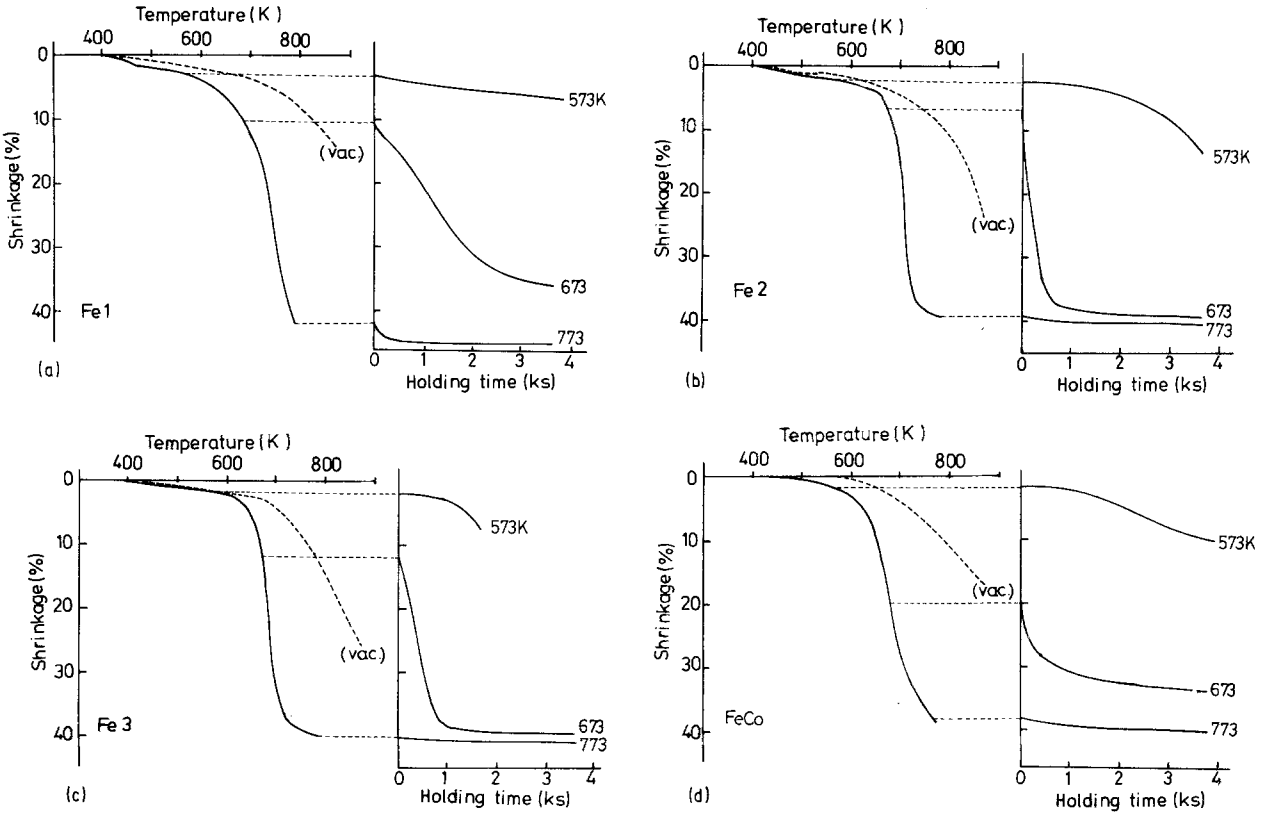

Figure 7 Linear shrinkage of the compacts during heating to fixed temperatures at a heating rate of 5 K min^{-1} (left-hand side), and during isothermal holding (right-hand side) in a stream of hydrogen. (– – –) The shrinkage in vacuum. (a) Fe1, (b) Fe2, (c) Fe3, and (d) FeCo.

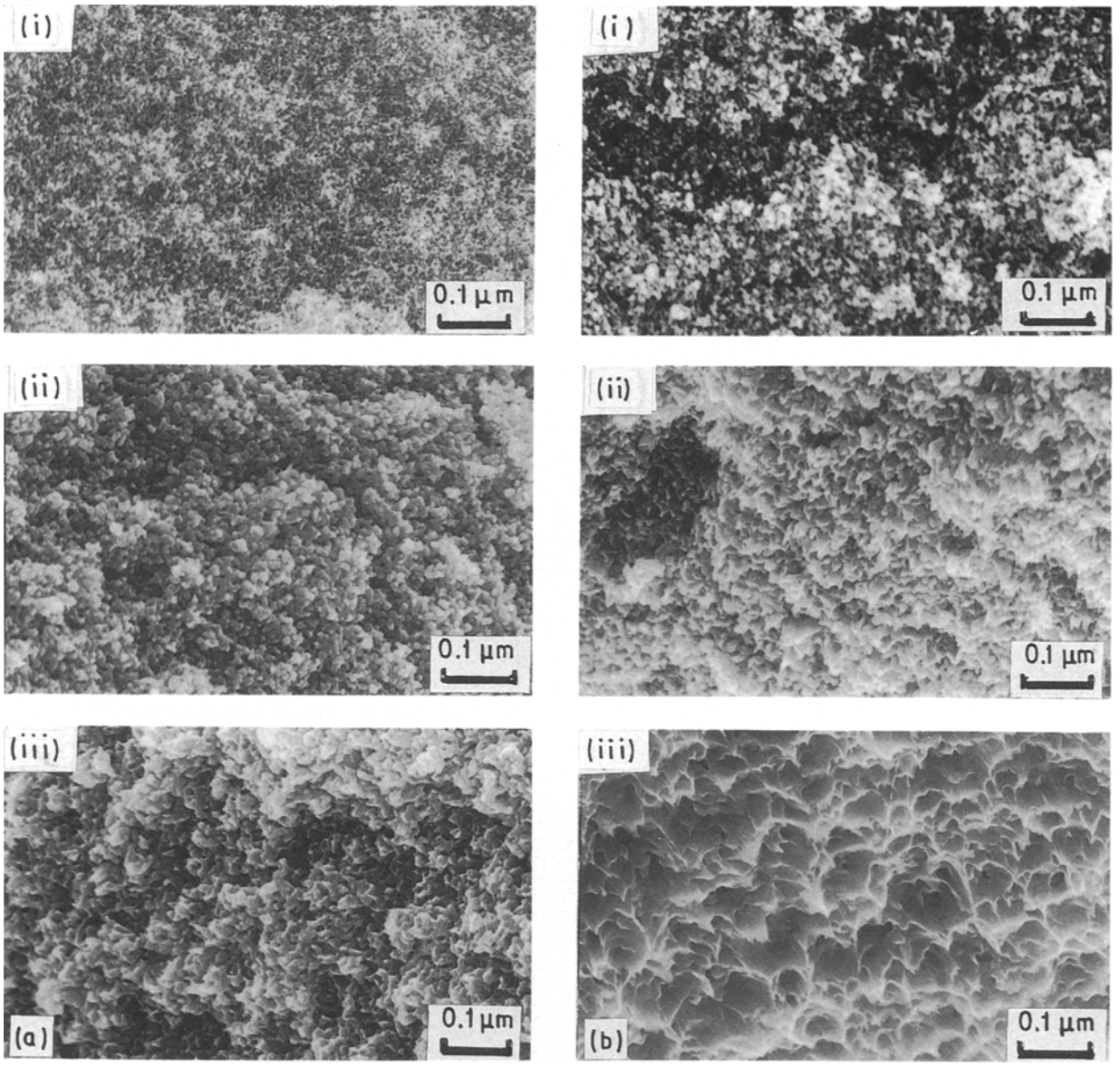

Figure 8 Fractured surfaces of the compacts sintered at (i) 573 K, (ii) 673 K, and (iii) 773 K. (a) Fe1, (b) Fe2, (c) Fe3, and (d) FeCo in a stream of hydrogen.

demonstrated that to compare the shrinkage curves with the variation of specific surfaces is a powerful method of predicting the sintering process [6]. In the sintering of the present UFPs, however, the effect of oxide phases on the sintering must be considered. Therefore, the crystallite sizes of the oxide and metal phases of the UFPs after sintering were measured by the X-ray broadening method. Fig. 15 shows the crystallite sizes of the oxide and metal phases after sintering at fixed temperatures for 1 h in vacuum, which were calculated from Equation 1. It is interesting that the growth of the metal particles is hindered by the presence of the surface oxide and that the growth of the oxide particles occurs initially.

The sintering diagrams in vacuum can be divided into three regions as summarized in Table III. In Fig. 2, the first region is that where a slight expansion is observed, the second that where a slight shrinkage is observed, the third that where a large shrinkage is observed.

In the first region (around 400 K), the specific surface areas increase (Fe1 and FeCo) or maintain constant values (Fe2 and Fe3). As seen in Fig. 10, large amounts of H_2O and CO_2 desorption from the surface oxide are observed. The crystallite sizes of the oxide and metal phases assume nearly constant values.

In the second region (450–700 K), the specific surface areas also decrease slightly. As described above, large amounts of oxide phase arise in this region. Moreover, the crystallite sizes of the oxide phase increase, but those of the metal phase remain constant. These results imply that the shrinkage is due to the sintering of the surface oxide.

In the third region (above 700 K), the crystallite sizes of both oxide and metal phases increase significantly. The grain growth of the UFPs is also observed as seen in Fig. 3.

On the other hand, the sintering shrinkage in a stream of hydrogen may be divided into two regions; the first region is that before reduction and the second

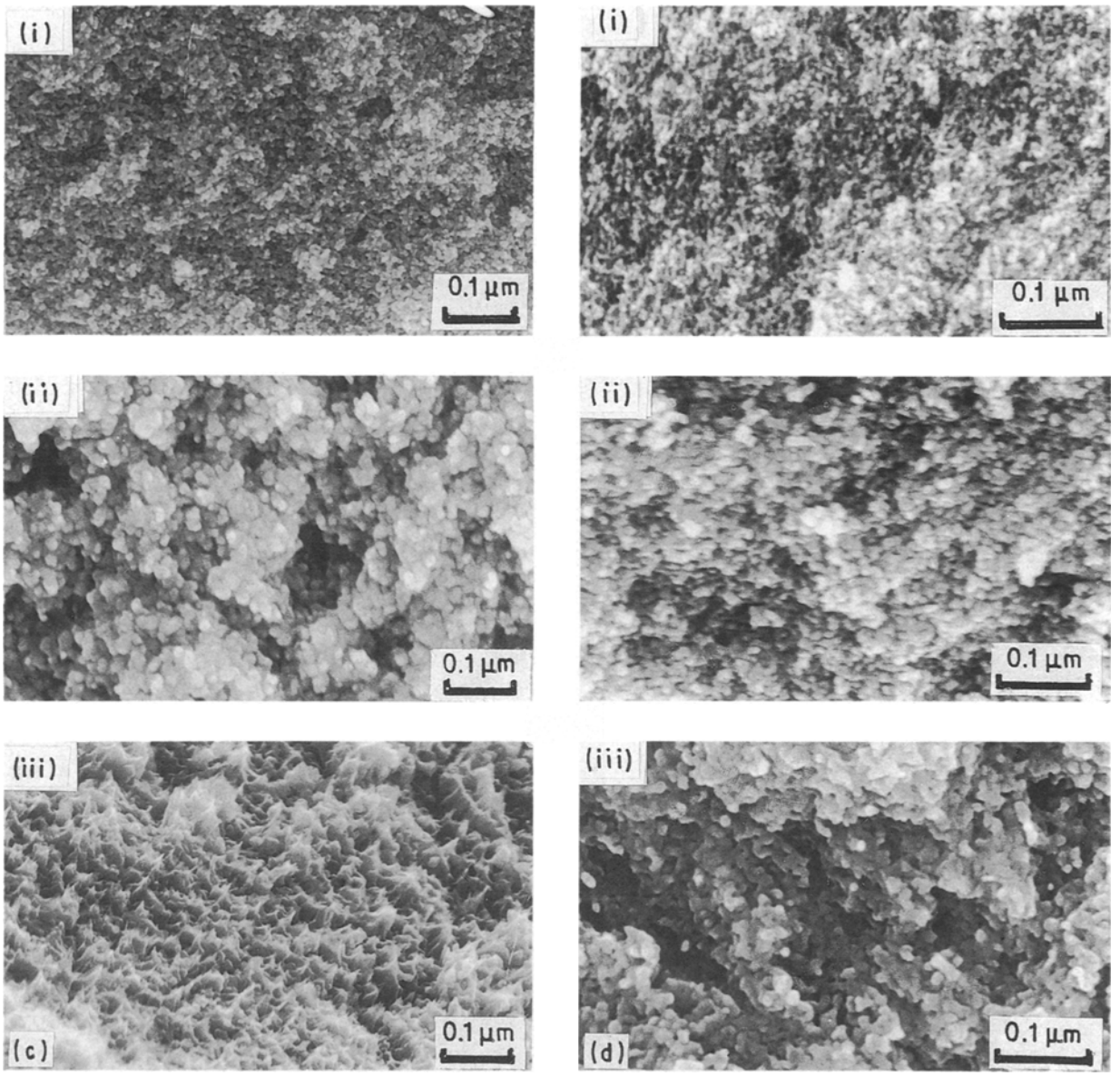

Figure 8 Continued

TABLE III Three regions of sintering in vacuum

Region	Shrinkage curve	Specific surface area	Crystallite size	
			Oxide	Metal
I	Slight expansion	Increase or constant	Constant	Constant
II	Slight shrinkage	Slight decrease	Increase	Constant
III	Large shrinkage	[a]	Increase	Increase

[a]Not measured.

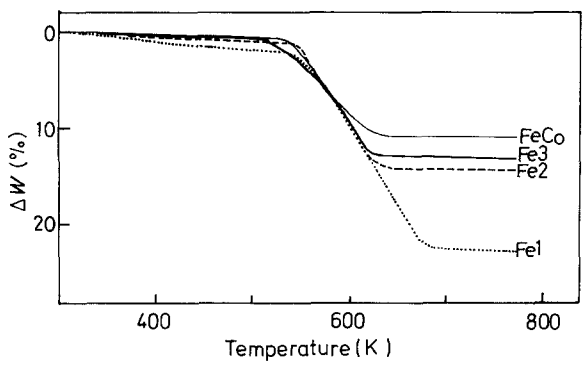

region that after reduction reaction. The shrinkage in the first region in a stream of hydrogen is basically similar to that in the second region in vacuum. Large shrinkage is observed in the second region. Grain growth is also observed on the micrograph of the fractured surface of the compacts. The iron UFPs sintered at 773 K, where the reduction reaction was

Figure 9 Thermogravimetry of the UFPs during heating at a rate of 5 K min^{-1} in a stream of hydrogen.

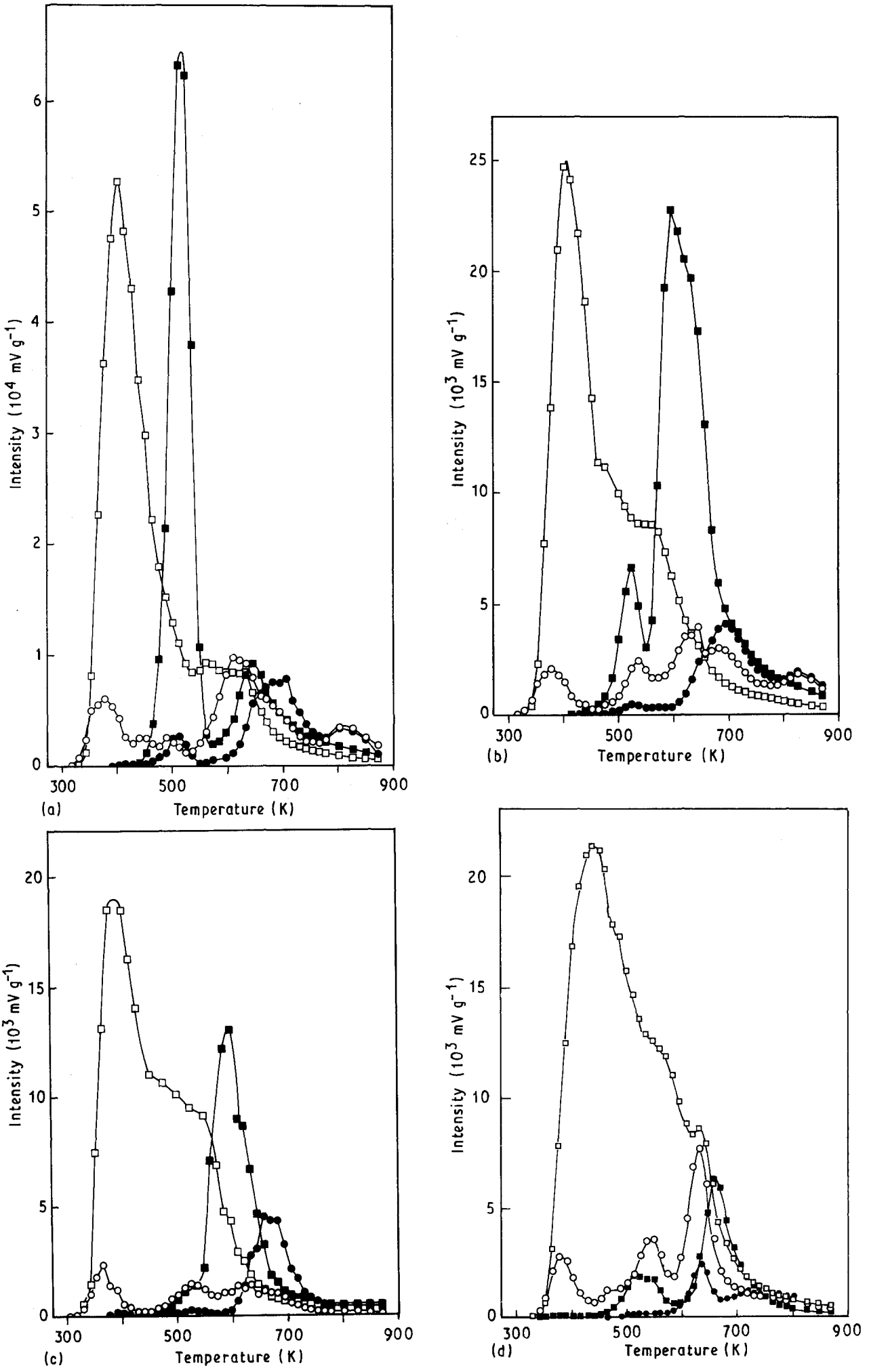

Figure 10 Temperature-programmed desorption (TPD) spectra of the ultrafine powders of (a) Fe1, (b) Fe2, (c) Fe3, and (d) FeCo at a heating rate of 5 K min^{-1} in a vacuum. (■) H_2, (□) H_2O, (●) CO, (○) CO_2.

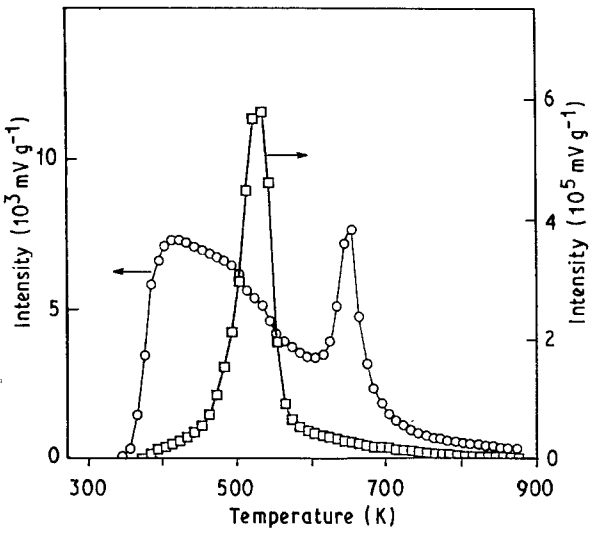

Figure 11 TPD spectra of γ-Fe_2O_3 (○) (99% purity, specific surface area 19.9 $m^2 g^{-1}$) and γ-FeOOH (□) (99% purity, specific surface area 15.4 $m^2 g^{-1}$) powders at a heating rate of 5 K min^{-1}.

completed, show dimple fracture as seen in Fig. 8. However, the FeCo UFPs sintered at 773 K show grain-boundary fracture because the FeCo is a brittle material. To increase ductility of the FeCo, we must hinder the grain growth, that is, sinter at lower temperatures probably under pressure.

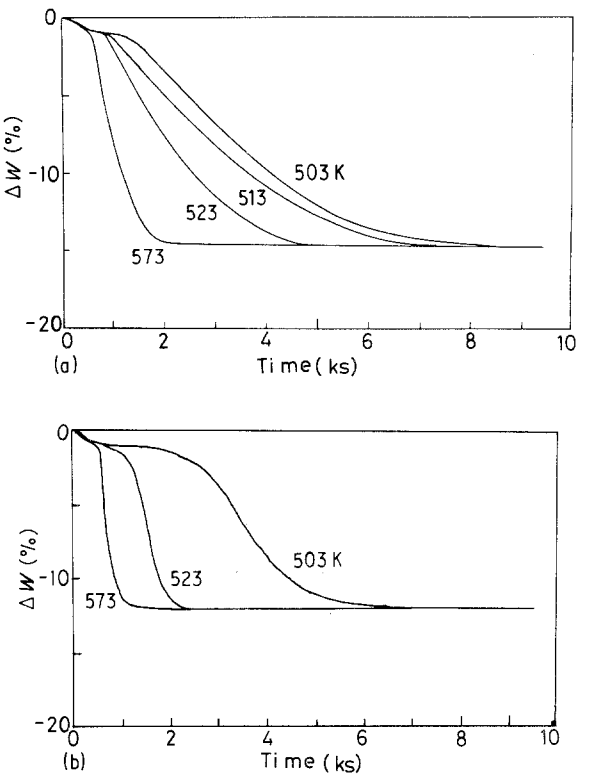

Figure 12 Weight losses of (a) Fe2 and (b) FeCo at fixed temperatures in a stream of hydrogen.

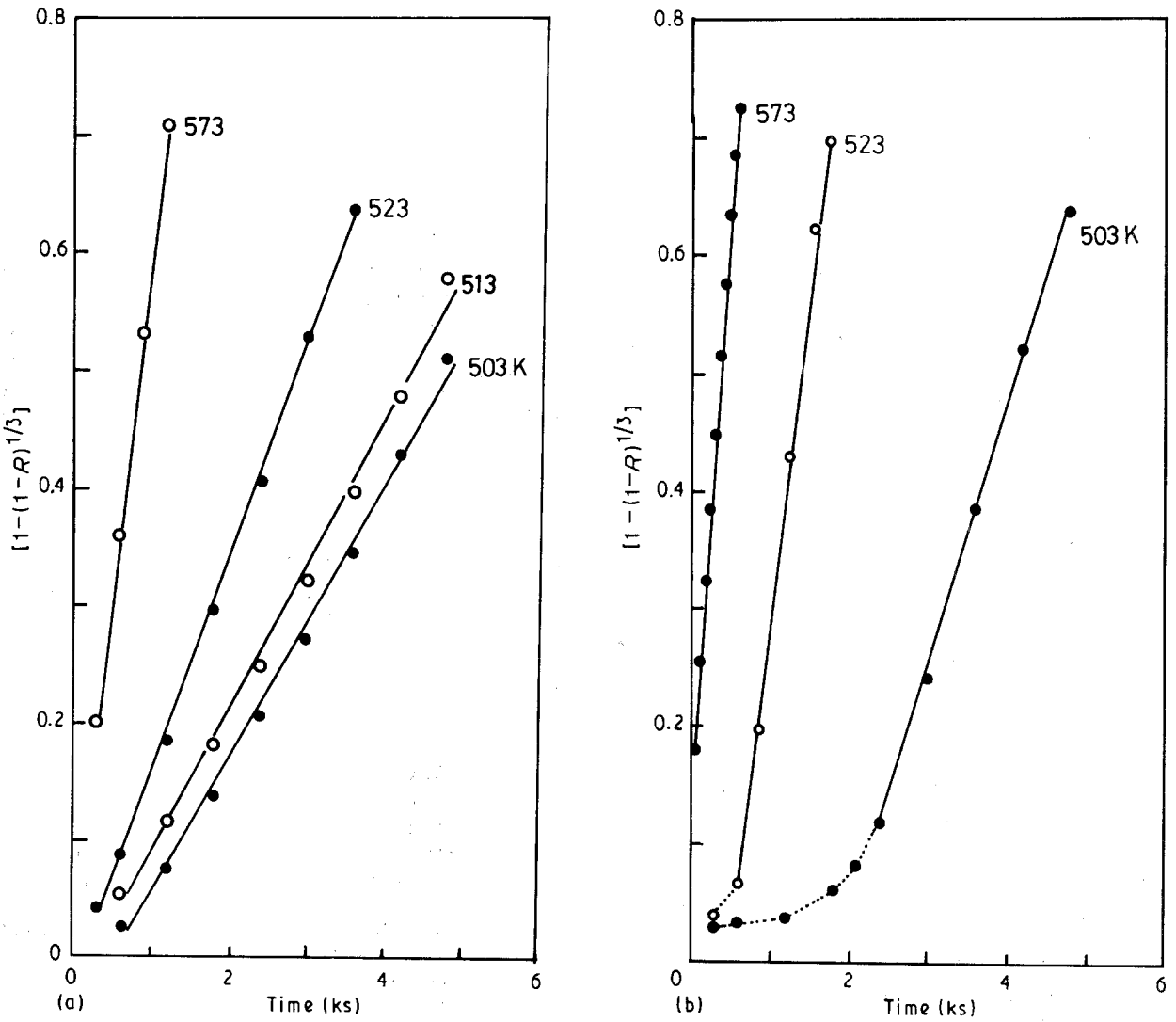

Figure 13 Relation of $[1-(1-R)^{1/3}]$ versus time. (a) Fe2, (b) FeCo.

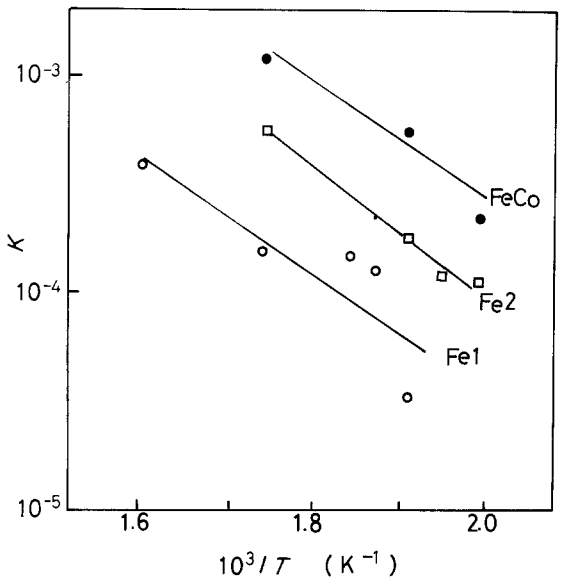

Figure 14 Arrenius plots of the reduction rate constant of the UFPs.

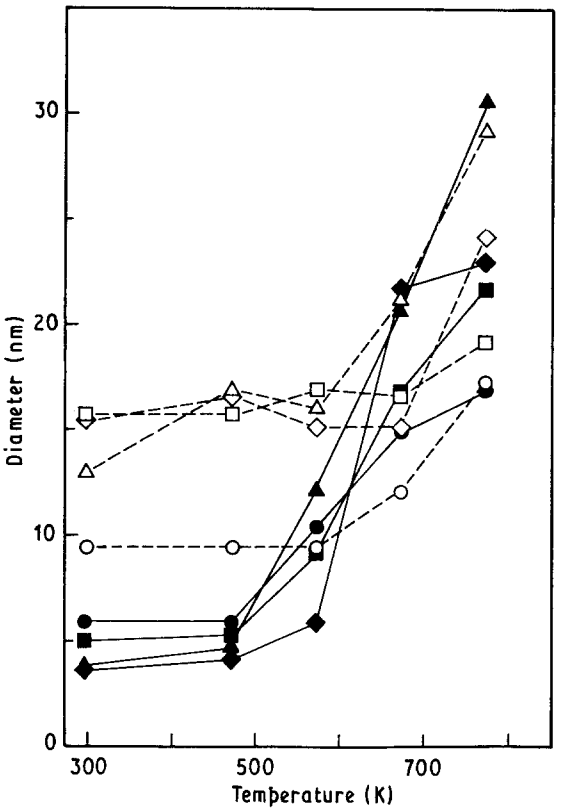

Figure 15 Variation of crystallite sizes calculated by Sherrer's equation after sintering at fixed temperatures for 1 h in vacuum. (○, ●) Fe1, (□, ■) Fe2, (△, ▲) Fe3, (◇, ◆) FeCo. Open symbols, metal; solid symbols, oxide.

In preparing the porous bodies consolidated by UFPs which have enough strength, two procedures can be proposed. One method is to sinter the compacts in the second region in vacuum or an inert gas atmosphere and then to reduce the surface oxide in a hydrogen atmosphere. However, the reduction rate might become slow because the grain size and density of the oxide phase increase during the above heat treatment. Because the reduction process is mainly rate-controlled by the interface reaction, the hydrogen pressure must be kept as high as possible to reduce the temperature and time of the reduction reaction. The other method is to sinter the compact in the first region in a hydrogen atmosphere before the large shrinkage occurs. The reduced bodies are so reactive that they must be treated in a controlled atmosphere.

5. Conclusions

1. The Fe UFPs contain mixtures of Fe_3O_4 and γ-Fe_2O_3 phases and in some case additional α-Fe_2O_3 phase. The FeCo UFPs contain spinel-type $(Fe,Co)_3O_4$ phase. Their properties are summarized in Tables I and II.

2. The oxide phase increases during heating of the UFPs in vacuum. The origin of the oxygen is discussed in connection with the TPD spectra and the following three reasons are considered:

(a) adsorbed gases on the oxide surface of the UFPs;

(b) decomposition of the hydroxide-like and carbonate-like compounds;

(c) reactions of the metal surface with the evolved water which originated from the adsorbed OH on the oxide surface of the UFPs and decomposition of hydroxide-like compounds (mainly oxyhydroxide).

3. The sintering diagrams in vacuum can be divided into three regions as shown in Table III. In the first region (below 450 K), large amounts of H_2O and CO_2 desorption were observed. In the second region (450–700 K), sintering of the surface oxide was observed. In the third region (above 700 K), a significant shrinkage and grain growth were observed due to sintering of both oxide and metal phases.

4. The sintering shrinkage and grain growth of the UFPs in a stream of hydrogen proceed significantly after the reduction reaction. The reduction reactions are rate-controlled by the interface reaction, and the activation energies of the reduction are 48–59 kJ mol^{-1}. The reduction rate of the UFPs depends on the oxidation level, where the more highly oxidized UFPs tend to the lower reduction rate.

Acknowledgements

We thank Drs K. Halada and Y. Muramatsu for their help in the use of the dilatometer and for helpful suggestions, and also Dr T. Furubayashi for Mössbauer measurements.

References

1. C. HAYASHI, R. UEDA and A. TASAKI (eds.), "Choubiryushi (Ultrafine Particles)" (Mita Shuppankai, Tokyo, 1988).
2. S. SAITO (ed.), "Choubiryushi Handobukku (Handbook of Ultrafine Particles)" (Fuji Tekunoshisutemu, Tokyo, 1990).
3. C. HERRING, *J. Appl. Phys.* **21** (1950) 31.
4. D. L. JOHNSON and I. B. CUTLER, *J. Amer. Ceram. Soc.* **46** (1963) 541, and references therein.
5. S. IWAMA, and K. HAYAKAWA, *Jpn J. Appl. Phys.* **20** (1981) 335.
6. Y. SAKKA, T. UCHIKOSHI and E. OZAWA, *J. Less-Common Metals* **147** (1989) 89.

7. Y. SAKKA, *J. Mater. Sci. Lett.* **10** (1991) 426.
8. X. ZHU, B. BIRRINGER, U. HERR and H. GLEITER, *Phys. Rev.* **B35** (1987) 9085.
9. R. W. SIEGEL and H. HAHN, in "Current trends in the physics of materials", edited by M. Yussouff (World Scientific, Singapore, 1988) p. 403.
10. K. HAYASHI and H. KIHARA, *J. Jpn Inst. Metals.* **50** (1986) 1089.
11. *idem, ibid.* **52** (1988) 343.
12. K. HAYASHI and H. ETOH, *ibid* **53** (1989) 221.
13. V. KEITH and M. G. WARD, *Cryogenics* (1984) 249.
14. H. FRANCO, J. BOSSY and H. GODFRIN, *ibid.* (1984) 477.
15. T. UCHIKOSHI, Y. SAKKA and E. OZAWA, *J. Jpn Inst. Metals* **53** (1989) 614.
16. Y. SAKKA, T. UCHIKOSHI and S. OHNO, *Proc. Jpn Congr. Mater. Res* **32** (1989) 104.
17. Y. SAKKA, T. UCHIKOSHI and E. OZAWA, *Mater. Trans. JIM* **31** (1990) 802.
18. T. UCHIKOSHI, Y. SAKKA and S. OHNO, *J. Jpn. Soc. Powder Powder Metall* **37** (1990) 508.
19. Y. SAKKA, S. OHNO and M. UDA, *J. Amer. Ceram Soc.* **75** (1992) 244.
20. E. FUCHITA, M. ODA and S. KASHU, in "Proceedings of the 7th International Conference on Vacuum Metal" (Iron Steel Institute of Japan, 1982) p. 973.
21. S. OHNO and M. UDA, *J. Chem. Soc. Jpn* (1984) 924.
22. K. HANEDA and A. H. MORRISH, *Surface Sci.* **77** (1978) 584.
23. B. D. CULITY, "Elements of X-ray Diffraction", 2nd Edn, (Addison-Wesley, MA, 1978) p. 102.
24. T. FURUBAYASHI, I. NAKATANI, and N. SAEGUSA, *J. Phys. Soc. Jpn* **56** (1987) 1855.
25. Y. SAKKA and T. UCHIKOSHI *J. Jpn Inst. Metals* **55** (1991) 219.
26. Y. SAKKA, *J. Mater. Sci. Lett.* **10** (1991) 987.
27. J. M. HERAS and E. V. ALBANO, *Appl. Surf. Sci* **17** (1983) 207.
28. T. UCHIKOSHI, M. YOSHITAKE, Y. SAKKA, T. FURUBAYASHI and I. YOSHIHARA, submitted to *J. Chem. Soc. Jpn.*
29. T. UCHIKOSHI and Y. SAKKA, *J. Jpn Inst. Metals.* **55** (1991) 558.
30. W. M. MCKEWAN, *Trans. Met. Soc. AIME* **212** (1958) 791.
31. M. TOKUDA, H. YOSHIKOSHI and M. OHTANI, *Tetsu-to-Hagane* **56** (1970) 1899.

Received 7 January
and accepted 2 June 1992